Inverse modeling of a single ring infiltration experiment: a key for analyzing unsaturated hydraulic properties of soils?

Michal Kuraz[a], Lukas Jacka[a], Johanna Ruth Blöcher[a], Matej Leps[b]

[a]*Czech University of Life Sciences Prague, Faculty of Environmental Sciences, Department of Water Resources and Environmental Modeling*
[b]*Czech Technical University in Prague, Faculty of Civil Engineering, Department of Mechanics*

Abstract

This contribution evaluates a possibility of identification of soil hydraulic properties (SHP) from inverse modeling of a single ring (hereafter SR) infiltration experiment. The SR experiment is a standard and robust dynamic field experiment. The steady state part of this experiment is traditionally used for an identification of saturated hydraulic conductivity. In this contribution, we explore the possibility of extending an applicability of this experiment for evaluating the unsaturated hydraulic parameters from an unsteady part of this experiment using inverse analyses of the governing flow motion equation.

The problem of SR infiltration is governed by qualisilinear Richards equation. We further present a methodology to avoid convergence issues with the nonlinear operator, originating from non-physical combinations of input parameters, which can be hard to avoid when automaticaly analyzing broad parameter space. With this methodology, we can answer (1) to what extent the well-known SR experiment is robust enough to provide a unique estimate of SHP parameters using the unsteady part of the infiltration experiment and (2) whether all parameters are vulnerable to non-uniqueness. We validated our methodology with synthetic infiltration benchmark problems for clay and sand, and applied on a real-world SR infiltration data. To evaluate non-uniqueness, local optima were identified and mapped using a modified genetic algorithm with niching, which is not possible with commonly used gradient methods.

Our results show the existence of multimodality in, both, the benchmark problems and the real-world problem. This is an important finding as local optima can be identified, which are not necessarily physical and also for systems that do not exhibit multimodal grain size distributions. The identified local optima were distinct and showed different retention and hydraulic conductivity curves. The most physical set of SHP could be identified with the knowledge of saturated water content, which makes it yet more obvious that expert knowledge is key in inverse modeling.

Keywords: soil hydraulic properties, inverse modeling, Richards equation, convergence issues, automatic calibration, computational issues in geosciences

1. Introduction

Soil hydraulic properties (hereafter SHP) are important for many hydrological models and engineering applications. The mountainous podzolic soil evaluated here is typical for the source areas of many major rivers in the Central European region. The top layer of the soil plays a key role in the rainfall-runoff process, because it is the top-soil that separates the rainfall into surface runoff and subsurface runoff.

Due to the rocks present and the dense root system of the covering vegetation, and due to the possible extension of the representative elementary volume, it is often impossible to collect undisturbed samples of top-soil for laboratory measurements in order to obtain the SHP parameters (Jačka et al., 2014). The SHP of the topsoil are therefore very difficult to measure directly (Fodor et al., 2011; Jačka et al., 2014).

In our study, the well-known single ring (hereafter SR) method was used to obtain experimental input data (cumulative infiltration) for inverse modeling. The SR infiltrometer is a widely accepted, simple, robust field method, which is able to measure the infiltration process, which affects the entire soil profile including the top-soil, and can sample a relatively large volume (depending on the diameter of the ring) (Cheng et al., 2011; Reynolds, 2008a). The SR infiltration experiment is an in situ experiment, which does not require soil samples to be collected, so the porous medium is kept relatively undisturbed. With the widely-used ring diameter of 30 cm, the affected porous media is far more representative than any soil sample we were able to collect. The top-soil can also be measured (with some alteration of the surface) using other well-known field infiltration methods, e.g. the tension infiltrometer or the well permeameter (Angulo-Jaramillo et al., 2000; Reynolds, 2008b).

The Richards equation (Richards, 1931) describes flow in variably saturated porous media. In order to model environmental processes and engineering applications with the Richards equation knowledge of the SHP is essential. SHP can be summarized by the soil water retention curve and soil hydraulic conductivity curve. In this contribution, the SHP are parametrized with the frequently used Mualem-van Genuchten model (van Genuchten, 1980). We refer to this model as REVG.

The identification of SHP from transient infiltration experiments has been a subject of numerous publications in past decades (Inoue et al., 2000; Lassabatère et al., 2006; Kohne et al., 2006; Xu et al., 2012; Bagarello et al., 2017; Younes et al., 2017). Inoue et al. (2000) reported a close correspondence between the SHP obtained from the inverse modeling of dynamic transient infiltration experiments with those obtained from steady-state laboratory experiments, where the uniqueness of the inverse model was preserved by considering the dynamically changing pressure head, water content and even tracer concentration.

The non-uniqueness of the REVG inverse model is already a very well-known issue, and has been described by a number of publications over the last decades (Kool et al., 1985; Mous, 1993; Hwang and Powers, 2003; Binley and Beven, 2003; Kowalsky et al., 2004; Nakhaei and Amiri, 2015; Kamali and Zand-Parsa, 2016; Peña-Sancho et al., 2017). Mous (1993) defined criteria for model identifiability based on the sensitivity matrix rank, however numerical computation of the sensitivity matrix, which is defined by the derivatives of the objective function,

2

often involves difficulties in managing truncation and round-off errors. Binley and Beven (2003) demonstrated on a real world case study of Sherwood Sandstone Aquifer that many different SHP parameters of macroscopic media can represent the layered unsaturated zone and provide acceptable simulations of the observed aquifer recharges. Mous (1993) explained that in case of the absence of water content data, the residual water content should be excluded from the identification to avoid non-uniqueness. However, Binley and Beven (2003) used a non-unique definition where both the unknown residual and saturated water content were considered. The definition of a unique inverse function for identification of macroscopic media was treated in (Zou et al., 2001), where the recommended approach was to assemble the objective function from transient data of the capillary pressure and from the steady state water content data.

A challenging issue is the treatment of the nonlinear operator of the Richards equation. Binley and Beven (2003) reported that 56% of the simulations were rejected during Monte Carlo simulations on a wide range of parameters, because of convergence problems. Their study did not mention explicitly why. We assume that these convergence issues originated from the nonlinear operator treatment.

The following questions arise:

- How can convergence issues be avoided, especially when the parameter range is wide?

- Is it possible to approximate the unsteady SR experiment using the REVG model, where the only unknown parameters represent the thin topsoil layer, by a unique set of parameters?

- If not, are all parameters vulnerable to non-uniqueness?

To answer these questions we employed a new calibration methodology.

1.1. Comment on system of units applied in this manuscript

Due to spatial and temporal scales of all model scenarios evaluated in this manuscript, instead of the base SI units we preferred to make use of *non-SI units accepted for use with the SI*. The length [L] will be always given in [cm], and the time [T] will be always given in [hrs].

2. Methodology

This section is divided into two parts. The first part, section 2.1, is focused on assembling the experimental data, which were later used as input for the inverse model. The site description, the reconstruction of the parameters of the SHP for the lower profiles, and the processing of the experimental data is given.

The second part of the methodology covers issues in the REVG inverse model. Section 2.2 derives governing equations and is given together with notes on the numerical stability of the REVG model for rotational symmetric problems. Section 9 discusses issues in creating the domain scheme and selecting appropriate boundary conditions, since it is not always easy to find an agreement between the mathematical model setup and physical
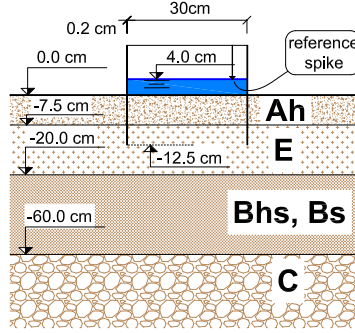
Figure 1: Scheme of the single ring infiltration experiment and the soil layers.

interpretation. Section 2.4.1 concludes with a description of the construction of the objective function, and the methodology of the automatic calibration.

2.1. Obtaining the input data for the inverse problem

2.1.1. Site description and assembling the experimental data

In this section a brief description of the conducted experiments is given. Since this contribution is focused on calibration methodology, we will significantly reduce the experimental data analyses. Complete description of this experiment including stastitical analyses of the experimental data is given in (Jačka et al., 2016).

The study site was located in the Šumava National Park, Czech Republic, and has been described in (Jačka et al., 2014). The location of the site in a map of Modrava 2 catchment is presented by Jačka et al. (2012). The soil profile is described by four different layers as seen on figure 1. Series of tension meter measurements of the top soil layer have been conducted on the site. The average soil suction head was estimated at 280 cm. If we further assume no-flow initial condition, then the average groundwater table can be roughly estimated at 280 cm below the surface. We are aware, that this assumption is a subject of a strong uncertainty. In a real world the soil suction head distribution is almost never hydrostatic (especially for this relatively humid mountainous region), as well as the tension meter data exhibit sever uncertainties. And so the estimated groundwater table is rather an overhead limit, which is already a significantly distant from the top-soil layer.

The SHP of the lower layers were identified by Guelph permeameter measurements (GP) with a methodology described by Jačka et al. (2014), and are presented in table 1.

Table 1: Soil hydraulic properties for the lower horizons.

horizon	GP experiment sites	θ_s [-]	α [cm^{-1}]	n [-]	K_s [cm.hrs^{-1}]	S_s [cm^{-1}]
E	28	0.46	0.046	1.741	1.584	0
Bhs + Bs	19	0.47	0.022	1.450	0.540	0
C	8	0.50	0.035	4.030	3.060	0

4

The experimental setup of the SR experiment was as follows. A steel ring 30 cm in inner diameter, 25 cm in length, and 2 mm in thickness was inserted into the soil to a depth of 12.5 cm, see figure 1. The depth of ponding was kept approximately at a constant level defined by a reference spike, which was placed 4 cm above the surface of the soil. The average experiment duration was 60 minutes.

For a simplicity and demonstrative purposes of our methodology, the experimental data will be represented here by a single average curve, which has been already constructed by Jačka et al. (2016). Jačka et al. (2016) has constructed the representative infiltration curve on basis of the Swartzendruber equation (Swartzendruber, 1987), which states that

$$I(t) = \frac{c_0 \left(1 - \exp\left(-c_1 \sqrt{t}\right)\right)}{c_1} + c_2 t, \tag{1}$$

where I is the cumulative infiltration [L], and $c_{0,1,2}$ are parameters. The Swartzendruber model describes one-dimensional infiltration into homogeneous medium, and is therefore not sufficient here. The Swartzendruber model was considered as an interpolating function. A statistical description of the Swartzendruber parameters, such as standard deviation, mean value, parameter variability, and their fitting quality is given in (Jačka et al., 2016), see datasets collected on site 3. According to this data paper the representative mean values are as follows: $c_0 = 5.130$ cm.hrs$^{-0.5}$, $c_1 = 1.13 \times 10^{-1}$ [-], and $c_2 = 1.858$ cm.hrs^{-1}. This parameter set together with (1) was used here to represent the input infiltration curve for demonstrating the calibration methodology proposed in this paper.

2.2. Mathematical model of the field infiltration experiment – governing equation

The field infiltration experiment is characterized by variably saturated conditions. The flux in porous media under variably saturated conditions can be expressed by the Darcy-Buckingham law (Buckingham, 1907)

$$\mathbf{q} = -\mathbf{K}(\theta)\nabla H, \tag{2}$$

where $\mathbf{q}$ is the volumetric flux [L.T^{-1}], H is the total hydraulic head [L] defined as $H = h+z$, where h is the pressure head [L], z is the potential head [L], θ is the water content [-], and $\mathbf{K}(\theta)$ is the unsaturated hydraulic conductivity [L.T^{-1}]; in general it is a second order tensor. The relation $\theta(h)$ is referred to as the retention curve (van Genuchten, 1980).

The geometry of the flow is inherently three-dimensional, but the domain dimension can be reduced by considering the axisymmetric geometry. The law of mass conservation for incompressible flow in cylindric coordinates is expressed as (Bear, 1979).

$$-\frac{\partial V}{\partial t} = \frac{\partial q_r}{\partial r} + \frac{q_r}{r} + \frac{\partial q_\alpha}{\partial \alpha} + \frac{\partial q_z}{\partial z}, \tag{3}$$

where V is the volume function [-], r is the radial coordinate, α is the angular coordinate, z is the vertical coordinate, and $q_{r,\alpha,z}$ is the volume flux [L.T^{-1}]. The ring infiltration experiment is characterized by rotational
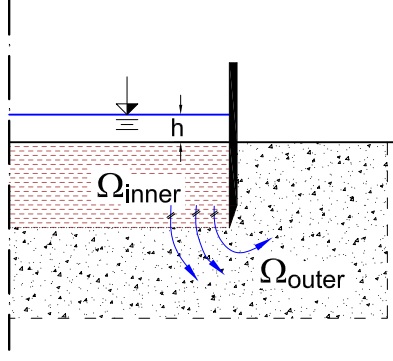
5

Figure 2: Scheme of the flow domain and the streamlines of infiltration experiment.

symmetric flow, so the angular derivative vanishes. Then the governing equation for variably saturated and rotational symmetric flow is obtained by substituting the flux in (3) by the Darcy-Buckingham law (2). Together with the consideration of linear elasticity (expressed by specific storage S_s) for a porous medium the variably saturated axisymmetric flow in isotropic media is governed by

$$\left(\frac{\mathrm{d}\theta}{\mathrm{d}h} + S_s \frac{\theta(h)}{\theta_s}\right)\frac{\partial h}{\partial t} = \frac{\partial K(h)\frac{\partial H}{\partial z}}{\partial z} + \frac{\partial K(h)\frac{\partial H}{\partial r}}{\partial r} + c(\mathbf{x})\frac{\partial H}{\partial r}, \tag{4}$$

where S_s is the specific storage [L^{-1}], θ_s is the saturated water content [-], $c(\mathbf{x})$ is the coefficient of the convection for r coordinate [T^{-1}], which is explained below, and the vector x is a vector of the spatial coordinates $\mathbf{x} = \left(\begin{smallmatrix} r \\ z \end{smallmatrix}\right)$.

If we consider the model of the infiltration experiment depicted in figure 2 with the entire flow domain $\Omega = \Omega_{inner} \cup \Omega_{outer}$, where Ω_{outer} is the flow domain outside the infiltration ring and Ω_{inner} is the flow domain within the infiltration ring, exactly as depicted in figure 4. It is then apparent that the streamlines inside subdomain Ω_{inner} are parallel, but the streamlines outside the infiltration ring (inside Ω_{outer}) are only axisymmetric. The convection coefficient $c(\mathbf{x})$ is then defined as follows

$$c(\mathbf{x}) = \begin{cases} 0, & \forall \mathbf{x} \in \Omega_{inner} \\ \frac{1}{r}K(h), & \forall \mathbf{x} \in \Omega_{outer}. \end{cases} \tag{5}$$

Note that we should avoid using the coordinates, where $r = 0$.

2.3. Domain setup

2.3.1. Initial and boundary condition setup

The computational domain scheme is depicted on figure 3. The initial condition was assumed as a steady state solution of (4) with the boundary $\Gamma_1 \cup \Gamma_2$ assumed as a no-flow boundary – thus the entire domain Ω was
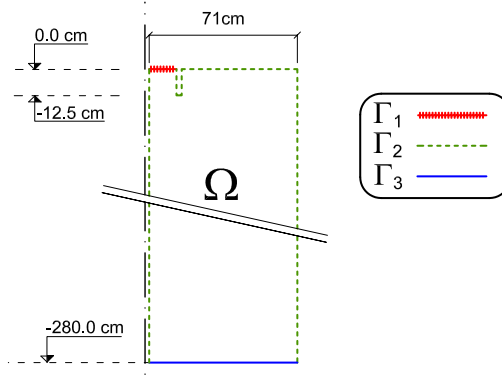
6

Figure 3: Scheme of the computational domain geometry and the domain boundaries.

considered to be in a hydrostatic state. The initial condition states that

$$H(x) = -280.0 \text{ cm}; \quad \forall x \in \Omega, \tag{6}$$

and thus $\frac{\partial h}{\partial z} = -1$.

The left hand side boundary was located at $r = 2$ cm, and the right hand side boundary was located at a distance $r = 73$ cm, which is 60 cm from the infiltration ring. The reasons for such position of the left hand side boundary will be explained in the section below.

The location of the top boundary was natural – the soil surface. Inside the ring, a Dirichlet condition defines the ponding depth; outside the infiltration ring a Neumann condition defines the no-flow boundary. The depth and definition of the bottom boundary was more problematic. We consider following commonly used options:

- the no-flow boundary (Neumann)

- the free drainage boundary (Neumann)

- the groundwater level - zero pressure head (Dirichlet)

It is apparent that the wetting front originating from our infiltration experiment affects the soil column only to a certain depth. Defining the Neumann no-flow boundary at a sufficient depth would probably not have a significant effect on the cumulative flux at the top Dirichlet boundary. At the same time, the only physically acceptable location of the no-flow boundary is the groundwater table. The second option – the free drainage boundary – would be completely incorrect for any depth, because we consider the initial condition to represent a hydrostatic state, and so

$$\frac{\partial h}{\partial z}(x) = -1, \quad \forall x \in \Omega. \tag{7}$$

7

The free drainage boundary condition, which is defined as

$$\frac{\partial h}{\partial \mathbf{n}}(x) = 0, \quad \forall (x, t) \in \Gamma_{\text{free drainage}} \times [0, T). \tag{8}$$

is in a conflict with the initial condition (since the outer normal vector $\mathbf{n} = \left(\begin{smallmatrix} 0 \\ -1 \end{smallmatrix}\right)$), and produces extra computational costs. The computed fluxes produced at the bottom boundary in the beginning of the simulation with such a boundary setup, originates from the initial and boundary condition mismatch, and has no physical meaning.

Physically correct boundary conditions for the bottom boundary is either the Neumann no-flow boundary at the impermeable layer or Dirichlet boundary both at the groundwater table. We chose a constant Dirichlet boundary condition. The minimal depth of the groundwater table is approximately -280 cm below the surface, and we assume that the water table remains constant during the experiment. With this particular setup the domain became extremely narrow and deep, see figure 4.

The locations of the domain boundaries are depicted in figure 3. The boundary conditions are specified as follows (with the reference level $z = 0$ located at the top boundary)

$$h(x, t) = 4 \text{ cm} \Rightarrow H(x, t) = 4 \text{ cm};$$
$$\forall (x, t) \in \Gamma_1 \times [0, T),$$
$$\frac{\partial H}{\partial \mathbf{n}} = 0; \ \forall (x, t) \in \Gamma_2 \times [0, T), \tag{9}$$
$$h(x, t) = 0 \text{ cm} \ \Rightarrow \ H(x, t) = -280.0 \text{ cm};$$
$$\forall (x, t) \in \Gamma_3 \times [0, T).$$

where T is the simulation end time [T], and $\mathbf{n}$ is the boundary normal vector.

2.3.2. Domain shape restrictions

It is well-known that sudden changes in domain shapes, spikes and discontinuities yield numerical difficulties (e.g. the Lipschitz boundary restrictions (Braess, 1997)). In order to avoid computational difficulties during the automatic calibration procedure the infiltration ring thickness was oversized to 2.5 cm, see figure 4. It is obvious that the real ring thickness is much smaller (in our case 2 mm), but using the real ring thickness yields possible numerical issues.

In order to evaluate the effect of such simplification we have solved the equation (4) accompanied with the initial condition (6) and boundary conditions (9) on domains with the oversized ring thickness of 25 mm and with the real ring thickness of 2 mm. The problem was solved on domains with two different mesh discretization setups – coarse mesh (1013 NDOFs with oversized ring and 1199 NDOFs with real ring thickness) and fine mesh (31848 NDOFs with oversized ring and 32328 NDOFs with real ring thickness). Details of different domains with different discretizations are depicted on figure 7. It is apparent that for coarse meshes the mesh density
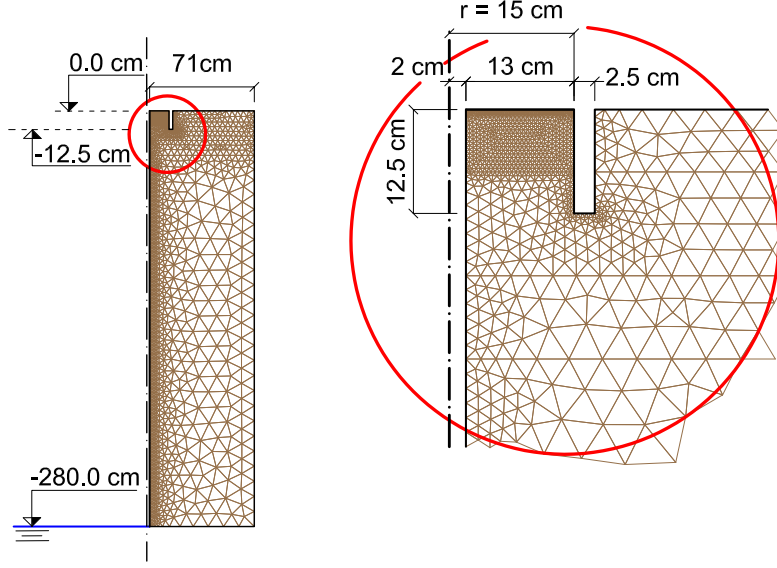
8

Figure 4: Scheme of the computational domain geometry and domain triangularization.

around the ring edge is governed by the domain shape. In order to validate the results the computation should be done on meshes, where the mesh density is not significantly influenced by the ring shape. Apparently, this is the case of the very fine meshes, where the mesh density Δx was equal to the ring thickness (2 mm). The domain triangulation was conducted with T3D mesh generator (Rypl, 2004), which has been successfully for a number of large engineering problems (Rypl, 2010; Kruis et al., 2002). Figure 6 depicts the relation between the difference $I_s(t) - I_r(t)$, where $I_r(t)$ [L] is the cumulative flux across the Dirichlet boundary for the domain representing the real ring thickness, and $I_s(t)$ [L] is the cumulative flux across the Dirichlet boundary on domain representing the oversized ring thickness. It is concluded that with the increased mesh density the difference $I_s(t) - I_r(t)$ vanishes. And so it becomes apparent, that oversizing the ring thickness does not significantly affect the fluxes through the top Dirichlet boundary, which is the only important part of the solution of (4) for our calibration process.

2.3.3. Stability restrictions of convection dominant problems

The equation (5) refers to coefficient of the first order derivative term in (4), and so the well known stability restrictions for the numerical solutions of the convection-diffusion problems appear here Christie et al. (1976). The Peclet number representing the numerical stability of convection-diffusion problems is defined as (Knobloch, 2008)

$$Pe = \frac{c\Delta x}{2D}, \qquad (10)$$

where c is the convection coefficient defined in (5), Δx is the discretization step, and D is the diffusion (for isotropic setup). Based on the definitions given above, equation (10) can be formulated as

$$Pe = \frac{\frac{1}{r}K(h)\Delta x}{2K(h)} = \frac{\Delta x}{2r}. \qquad (11)$$
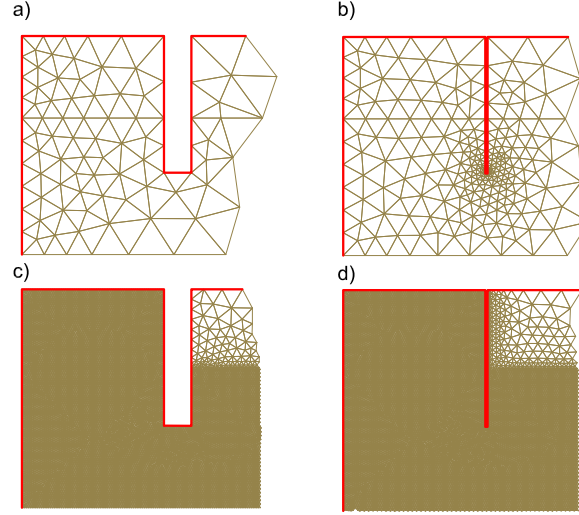
9

Figure 5: Details of domains with the oversized ring thickness and the real ring thickness discretized with different triangulation densities. Details a) 1013 NDOFs, b) 1199 NDOFs, c) 31848 NDOFs, d) 32328 NDOFs.
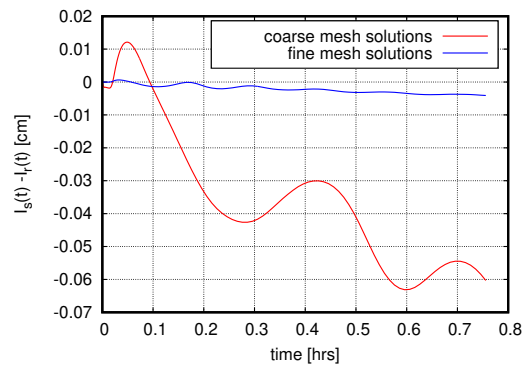

Figure 6: Difference between the cumulative infiltration on domain with real ring thickness I_r and the oversized ring thickness I_s. It is apperent, that with the increased mesh density this difference vanishes.

Since our mesh is triangular, Δx can be roughly assumed to be the greatest triangle altitude (since we assume some mesh quality properties). Then a sufficient distance from the axis of anisotropy is such that the Peclet number is sufficiently low. If we want to make our computation free of the well known spurious oscillations (Christie et al., 1976; Roos et al., 1996), a sufficiently low Peclet number $Pe \leq 1$ is required. Therefore, the distance from the axis of anisotropy is given by the domain discretization step at the left hand side boundary. The selected discretization step at the left hand side boundary was assumed as $\Delta x = 2$ cm. The domain was therefore detached by 2 cm from the axis of anisotropy, and thus the Peclet number was 0.5 only. This simplification must be again validated. However, compared to the oversized ring thickness, it is impossible to numerical model domains, where $r_{min} = 0$. And so three different setups, where the domain was detached for $r_{min} =0.2$, 1.0, and 2.0 cm from the center of anisotropy, were tested. In order to maintain the Peclet number on equal level, the mesh density Δx at the left hand side boundary should be equal to r_{min}. It is apparent, that compared to the previous case, where we were evaluating the oversized ring thickness, changing the location of the left hand side boundary will significantly affect the mesh size, as depicted on figure 7. In order to obtain comparable data, three different domains with r_{min}=0.2, 1.0, and 2.0 cm were triangularized with equal mesh densities given by the lowest r_{min} (in order to obtain comparable data). It turns out, that for r_{min}=2.0 cm the Peclet number (11) was $Pe = 0.05$, and the mesh size was 10851 NDOFs, for r_{min}=1.0 cm the Peclect number was $Pe = 0.25$, and the mesh size was 100036 NDOFs , and for $r_{min} = 0.2$ cm the Peclet number was $Pe = 0.5$, and the mesh size was 10156 NDOFs. Since the Peclet numbers are already very low, the solutions are free of spurious oscillations, and can be compared. Please note, that the mesh sizes with decreasing r_{min} doesn't increase monotonously, since the mesh is non-uniform and different mesh density and domain shape configurations lead to different triangularizations.

Similarly to the previous section 2.3.2, the equation (4) accompanied with the initial (6) and boundary conditions (9) was solved on three different domains with r_{min} =0.2, 1.0, 2.0 cm. The figure 8 depicts the difference between the cumulative volumetric flux across the top Dirichlet boundary for the domains with r_{min} offset 2.0 cm and 1.0 cm, and with r_{min} offset 2.0 cm and 0.2 cm. It is apparent, that while decreasing the offset with ratios 0.5 and 0.1 the differences between the cumulative fluxes maintain similar order of magnitude. The differences probably originate from different domains triangularizations, and are below the data resolution originating from in-situ experimental conditions.

2.4. Optimization

2.4.1. Objective function

In this section the methodology for identification of the SHP parameters from the Richards equation will be presented. Since the parameters will be identified using a stochastic method, we have to introduce a range for each parameter. The ranges for the SHP are specified in table 2. These initial ranges are very broad, since we are trying to explore a possible non-uniqnuess of this inverse model even beyond physically acceptable ranges.

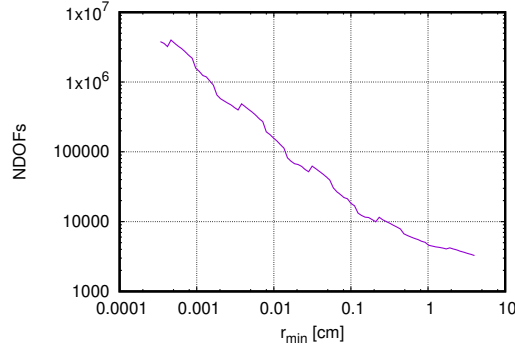The objective function is defined in the following paragraph.

Figure 7: Relation between the distance from the axis of anisotropy (r_{min}) and the mesh size (NDOFs), while maintaining the Peclet number of convective dominance (11) at constant level. Over 100 meshes with T3D mesh generator Rypl (2004) were generated for this plot, the relation is not monotoneous, since different mesh densities yield different triangularizations.

Figure 8: Relation between the distance from the axis of anisotropy (r_{min}) and the mesh size (NDOFs), while maintaining the Peclet number of convective dominance (11) at constant level. Over 100 meshes with T3D mesh generator Rypl (2004) were generated for this plot, the relation is not monotoneous, since different mesh densities yield different triangularizations.
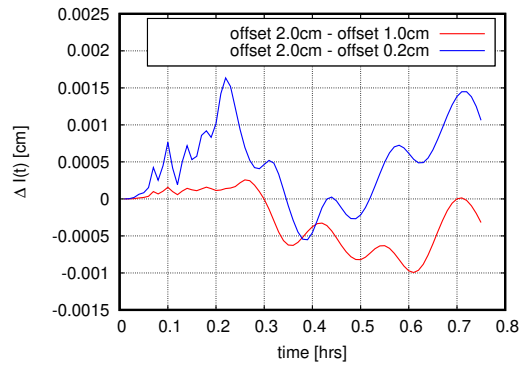
Table 2: Ranges of SHP ($\mathbf{p}_{max}$ and $\mathbf{p}_{min}$) for identifying the SHP in the top-soil layer for *refinement level r_f = 0*. Note that the initial ranges are extremely broad especially for the saturated water content θ_s. This broad range was selected in order to explore the uniqnuess of the REVG inverse model of SR experiment even beyond the physically acceptable solutions.

θ_s [-]	α [cm^{-1}]	n [-]	K_s [cm.hrs^{-1}]	S_s [cm^{-1}]
$0.25 - 0.90$	$1 \times 10^{-4} - 5.000 \times 10^{-2}$	$1.05 - 4.5$	$0.300 - 300.0$	$0.0 - 0.1$

Let $\bar{I}(\mathbf{p}, t)$ be the cumulative infiltration obtained from solving the mathematical model (4) bounded by the initial and boundary conditions defined in section 9 for a certain vector of SHP parameters $\mathbf{p}$ considered as

$$\bar{I}(\mathbf{p}, t) = \frac{\int\limits_0^t \int\limits_{\Gamma_1} -K\frac{\partial H}{\partial \mathbf{n}}(t)\mathrm{d}\Gamma_1 \mathrm{d}t}{\int\limits_{\Gamma_1} \mathrm{d}\Gamma_1}. \tag{12}$$

Let $I(t)$ be the cumulative infiltration given by (1) with parameters given in section **??**. Then the objective function was defined for three different criteria in order to avoid ill-posed objective function definition.

Both $\bar{I}(\mathbf{p}, t)$ and $I(t)$ are continuous functions. Note please, that this is not a standard configuration. The objective functions were then defined as follows:

I. First criterion Ψ_1 was defined as L_2 norm of the difference between the experimental and model data and thus

$$\Psi_1(\mathbf{p}) = \frac{\sqrt{\int\limits_0^{T_{end}} \left(\bar{I}(\mathbf{p}, t) - I(t)\right)^2 \mathrm{d}t}}{T_{end}}, \tag{13}$$

where T_{end} is the final simulation time [T], which is indeed the root mean square error (RMSE) for continuous functions.

II. Second criterion was the L_∞ norm of the difference between the experimental and model data and thus

$$\Psi_2(\mathbf{p}) = \sup\left(\sqrt{\left(\bar{I}(\mathbf{p}, t) - I(t)\right)^2}\right), \quad t \in (0, T_{end}). \tag{14}$$

III. Third criterion was considered as the difference between the infiltration rates (final derivatives) between the model data and the experimental data

$$\Psi_3(\mathbf{p}) = \sqrt{\left(\frac{\mathrm{d}\bar{I}(\mathbf{p}, T_{end})}{\mathrm{d}t} - \frac{\mathrm{d}I(T_{end})}{\mathrm{d}t}\right)^2}. \tag{15}$$

We conducted multi-objective optimization. However, it is apparent that minimizing the objective function (13) also minimizes the objective functions (14) and (15), and so we have introduced here a multiobjective

definition with non-competing objective functions.

The usage of multi-objective optimization to solve inverse problems is three-fold: (i) to speed-up the convergence in case of non-competing objective functions, (ii) to find out the trade-off among the measurements' errors in case of several experiments and/or measurements and (iii) to enable easy post-processing without using any weighting in the second case.

The multi-objective case (i) for parameter estimation is inspired by Knowles et al. (2001) where the authors expand the single-objective problem to the multi-objective space by replacing the original objective with a set of new objectives or new objectives are added to the original one. The idea is to give an algorithm more freedom to explore the search space and, therefore, decreases the probability to be trapped in a local extreme. Although superfluous at the first view, in many cases the speed-up to the original single-objective optima was higher in the multi-objective case. Similar idea is behind *helper* objectives Jensen (2004), however, the computational advantage of the multi-objective application is problem-dependent, see Vitingerova (2010) and references therein.

The objections for the (ii) case is as follows. In case of several experiments and/or measurements the goal is to minimize a discrepancy between model(s) output and measurements, usually expressed in a form of error functions. Perfect fit then corresponds to zero errors. The usual scenario assumes correlation and/or independency among those error functions, applies weighting and thus creates the single-objective optimization problem.

First, many classical material models have independent sets of parameters for different phenomena and thus the error functions are non-competing. However, in many models, especially phenomenological ones, some parameters influence several model's outputs and therefore, they are dependent and the objectives can be competing.

Second, it must be pointed out that the perfect fit should not exist for real data because of the generalization and measurements errors. The zero error is usually result of insufficient experimental data and/or too many parameters (the degrees of freedom) of the used model leading to *overfitting*, see Weise et al. (2009). Thus the individual error functions can be minimized towards the zero individually but not jointly. The multi-objective approach then enables (ii) to find out the trade-off among individual errors and (iii) to set up the importance of the individual measurements *a posteriori* after the search, see e.g. Kuraz et al. (2010) or Gong et al. (2015) for such applications.

2.4.2. Optimization algorithms

Genetic algorithm. In this contribution we used the modified genetic algorithm GRADE (Ibrahimbegović et al., 2004; Kucerova, 2007) supported by niching method CERAF (Hrstka and Kucerova, 2004) enhancing the algorithm with memory and restarts. GRADE is a real-coded genetic algorithm combining the ideas of genetic operators: cross-over, mutation and selection taken from the standard genetic algorithm and differential operators taken from differential evolution. When GRADE converges, the current position of the optimization algorithm is marked as a local extreme and a forbidden area is built around it in order to forbid the optimization algorithm to fall into the same local extreme again. The main setting of the optimization procedure was as follows: the population of the genetic algorithm contains 30 independent solutions, the whole identification stops after 20.000

14

objective function evaluations and a local extreme was marked after 600 evaluations without any improvement.

GRADE project is capable for multi-objective definition for the objective function, which is achieved with so-called Average Ranking (AR) (Leps, 2007). It sums ranks of the objective functions instead of the objective functions' values. Therefore, no weights are needed, however, the Pareto-dominance is not preserved as described in Vitingerova (2010). An application of the AR algorithm to parameters identification can be found in Kuraz et al. (2010).

Gradient algorithm. Since achieving the fully converged solution with genetic algorithms is often cumbersome, the genetic algorithm was used here as an estimator of the initial condition for further gradient parameter search on narrow ranges. For gradient optimization we made use of Newton's method with box-constraints (Byrd et al., 1995), implemented in R environment (R Core Team, 2017).

2.5. Numerical solution and computational issues

Equation (4) was implemented into the DRUtES library (Kuraz et al., 2008). It is an object-oriented library written in Fortran 2003/2008 standard for solving nonlinear coupled convection-diffusion-reaction type problems. The problem was approximated by the linear finite element method for spatial derivatives and Rothe's method for temporal derivatives. The nonlinear operator was treated with the Schwarz-Picard method – an adaptive domain decomposition (*dd*-adaptivity) – with the ability to activate and deactivate subregions of the computational domain sequentially (Kuraz et al., 2013a, 2014, 2015).

The domain was non-uniformly discretized by a triangular mesh. The smallest spatial step was considered for the top layers inside the infiltration ring, close to the Dirichlet boundary. The mesh is depicted on figure 4. The minimum spatial length was 0.5 cm, and the maximum spatial length was 20 cm. The domain was discretized with 2097 nodes and 3861 elements. The coarse mesh for the *dd*-adaptivity method was a uniform quadrilateral mesh with elements 17.75×28.0 cm, i.e. a total of 40 coarse elements and 55 nodes. The purpose of the coarse mesh is to organize the elements of the domain triangularization into so-called clusters, which form a basic unit for the adaptive domain decomposition used here for solving the nonlinear problem, details can be found in (Kuraz et al., 2015).

The spatial and temporal discretization of (4) leads to sequential solutions of systems of non-linear equations, see e.g. (Kuraz et al., 2013a). The system was linearized as discussed in Kuraz and Mayer (2013); Kuraz et al. (2013b), and so the numerical solution requires an iterative solution of

$$\mathbf{A}(\mathbf{x}_l^k)\mathbf{x}_l^{k+1} = \mathbf{b}(\mathbf{x}_l^k), \tag{16}$$

where k denotes the iteration level, and l denotes the time level, until

$$\|\mathbf{x}_l^{k+1} - \mathbf{x}_l^k\|_2 < \varepsilon, \tag{17}$$

15

where ε is the desired iteration criterion. It is apparent that the number of required iterations depends on the ε criterion.

The method (16) degenerates into a kind of semiexplicit approximation if the error criterion ε was "infinitely huge" (it means taken from the extended real numbers, $\varepsilon \in \overline{\mathbb{R}}$, and assigned as $\varepsilon = +\infty$). This semiexplicit approximation is denoted as

$$\mathbf{A}(\mathbf{x}_{l-1})\mathbf{x}_l = \mathbf{b}(\mathbf{x}_{l-1}). \tag{18}$$

This semiexplicit method always requires just a single iteration. With a short time step the method converges to the exact solution. For inappropriate time steps, the method diverges from the exact solution faster than the method (16). Nonetheless, the method (18) is free of possible issues related to the convergence of the nonlinear operator.

3. Automatic calibration methodology

We address possible difficulties with convergence of the linearized discrete system (16) for certain combinations of SHP parameters during the automatic calibration, as discussed by Binley and Beven (2003). Moreover, we address the problem of multimodality when the initial range of SHP parameter is broad as in table 2. It is known that inaccurate approximation of the capacity term (time derivative term) yields inaccurate mass properties (Celia et al., 1990) and are aware of the possible impact of spatial and temporal discretization on the identified SHP values.

Following the concerns about effects of the numerical treatment on the identified SHP, we propose an automatic calibration methodology depicted in figure 9. Details are given in the following algorithm scheme. In brief, the proposed method uses less accurate, but fast and convergence-issue-free numerical technique, to identify (several) promising parameter regions. To avoid the influence of the numerical solver setup, the SHP estimate is consequently updated in each parameter region with an improved numerical treatment of the Richards equation solver. It is presumed that the inverse model solution is non-unique on the initial broad parameter range, but unimodal on the narrow region(s), which are subsequently investigated.

Let us define the following nomenclature:

---

r_f – "refinement level", the problem is treated with different spatial and temporal discretization setups, each setup is denoted by value of r_f index,

i_e – local extreme index,

$\mathbf{p}$ – vector of SHP parameters, vector contains the values of α, n, θ_s, K_s, S_s,

16

$\mathbf{p}_{max,min}^{r_f}$ – maximal, resp. minimal values of SHP parameters defining a parameter range for a certain refinement level r_f,

$\mathbf{p}_{max,min}^{i_e,r_f}$ – maximal, resp. minimal values of SHP parameters defining a parameter range for a certain refinement level r_f in a certain vicinity of a local extreme i_e,

$\Delta(\mathbf{x})$ – spatial discretization (mesh density, mesh is non-uniform).

The calibration algorithm is described as follows:

[I.] Do initial calibration with genetic algorithm GRADE (Ibrahimbegović et al., 2004) and with semiexplicit method (18) ($\varepsilon \rightsquigarrow +\infty$), r_f=0, vectors $\mathbf{p}_{max,min}^{r_f}$ are taken from table 2

[II.] Create sequence of vectors $\bar{\mathbf{p}}_{r_f}^{i_e}$. Please note that these extremes are typically parameter sets in a vicinity of the objective function minimum.

- **If** the problem is multimodal
  - **then** $i_e > 1$,
  - **else** $i_e = 1$.

[III.] For each vector $\bar{\mathbf{p}}_{r_f}^{i_e}$ conduct gradient optimization using Newton's method with box-constraints (Byrd et al., 1995) on parameter ranges $\mathbf{p}_{max}^{i_e,r_f} = 1.1\bar{\mathbf{p}}_{r_f}^{i_e}$ and $\mathbf{p}_{min}^{i_e,r_f} = 0.9\bar{\mathbf{p}}_{r_f}^{i_e}$, where the initial estimate is obtained from the genetic algorithm solution $\bar{\mathbf{p}}_{r_f}^{i_e}$, so that the converged solution $\mathbf{p}_{r_f}^{i_e}$ is ensured.

[IV.] Do validation:

(a) **select** local extremes with good fitting qualities,

(b) **increase** $r_f = r_f + 1$ as follows

$$\Delta(\mathbf{x})^{r_f} = \frac{\Delta(\mathbf{x})^{r_f-1}}{2},$$
$$\varepsilon^{r_f} = 10^{-3} \text{ cm} \quad \text{if } r_f = 1,$$
$$\text{else} \quad \varepsilon^{r_f} = \frac{\varepsilon^{r_f-1}}{10}, \quad (19)$$
$$t_{init}^{r_f} = \frac{t_{init}^{r_f-1}}{10} \text{ hrs.}$$

(c) **create** a response plot of (13) for current r_f and $r_f - 1$ in the neighborhood defined as

$$\mathbf{p}_{max}^{i_e,r_f} = 1.25\mathbf{p}^{i_e},$$
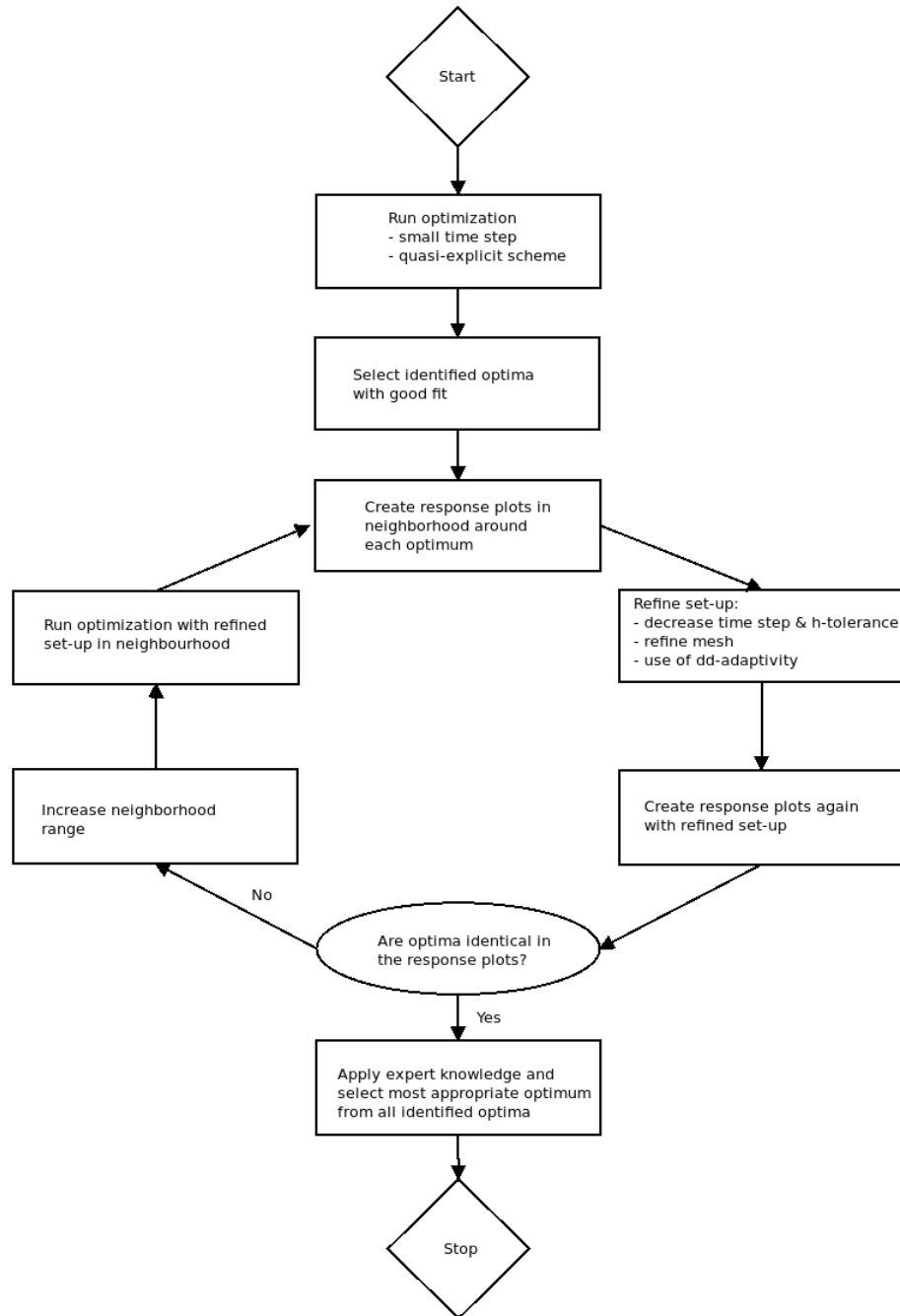$$\mathbf{p}_{min}^{i_e,r_f} = 0.75\mathbf{p}^{i_e}. \quad (20)$$

Figure 9: The proposed methodology for the automatic calibration avoiding effects of numerical treatment for the identified SHP values.

18

(d) **Validation methodology:**

    i. Visually **inspect** response plots for the selected local extreme i_e created with discretization r_f and $r_f - 1$.

    ii. **If** the response plots differ significantly,

- **then redefine** the parameter range as specified in (20), **return** to **[III.]**, start a **gradient optimization**, where the initial estimate is $\mathbf{p}_{r_f-1}^{i_e}$. **For each** local extreme i_e new sets of vectors $\mathbf{p}_{r_f}^{i_e}$ will be generated, **go to [IV.]** and **proceed new validation**.

- **else exit** the calibration process.

4. Results and discussion

This section begins with a simple synthetic problem with known exact solution, which is given here to test the multimodality of this class of Richards equation inverse model, to provide a support for the methodology given in section 3. Later, we continue in section 4.2 with presenting our real world problem example, where we present our parameter estimate for the top soil organic horizon, obtained from the methodological approach explained above in 3.

4.1. Synthetic problem

The purpose of this benchmark example was to demonstrate, whether this class of problem – identification of SHP parameters from cumulative flux measured at Dirichlet boundary – can be affected by multimodality.

For simplicity only a one-dimensional Richards equation problem was considered here. Dirichlet boundary conditions were presumed for both boundaries. The model setup state as follows. Computational domain was $\Omega = (0, 100 \, \text{cm})$, and the boundary and initial conditions stated as follows

$$
\begin{aligned}
h(x,t) &= 0 \, cm, & \forall (x,t) \in \Gamma_{bot} \times t \in [0, T_{end}) \\
h(x,t) &= 0 \, cm, & \forall (x,t) \in \Gamma_{top} \times t \in [0, T_{end}) \\
H(x,t_0) &= 0 \, cm, & \forall x \in \Omega,
\end{aligned}
\tag{21}
$$

where $\Gamma_{bot} = 0.0$ cm, $\Gamma_{top} = 100.0$ cm, and $T_{end} = 10^{-1}$ hrs. Two distinguished soil types were considered here – clay loam and sand, the parameters were obtained from (van Genuchten et al., 2009).

The computational domain Ω was uniformly discretized with $\Delta x = 0.5$ cm, the initial time step was $\Delta t = 10^{-7}$ hrs, and the error criterion from (17) for solving the nonlinear system (16) was $\varepsilon = 10^{-3}$ cm.

The reference solutions both for sand and gravel media were obtained from cumulative flux over the top Dirichlet boundary Γ_{top}.

For the given reference solutions the inverse modeling algorithm described in section 2.4.2 was employed for searching the original SHP parameters in broad ranges given in table 2. In order to avoid effects of numerical

19

Table 3: Results of the synthetic problem. The grey highlighted rows refer to the physically acceptable solution of this benchmark inverse problem, and the red highlighted rows contain the exact solution of this inverse problem.

			parameters				RMSE error
			α [cm^{-1}]	n [-]	θ_s [-]	K_s [cm.hrs^{-1}]	
clay loam	exact solution		**0.019**	**1.31**	**0.41**	**6.24**	
	identified solutions	1	0.020	1.321	0.395	6.226	4.787×10^{-2}
		2	0.012	1.050	0.250	7.011	2.830×10^{-1}
		3	1.280×10^{-4}	1.146	0.900	94.904	3.724×10^{-1}
sand	exact solution		**0.145**	**2.68**	**0.43**	**29.7**	
	identified solutions	1	0.039	1.050	0.250	35.563	2.978×10^{-2}
		2	0.026	1.087	0.587	37.877	2.406×10^{-2}
		3	0.154	2.654	0.460	30.145	2.199×10^{-2}

Table 4: Identified local extremes of Pareto front during the first run of parameter search procedure.

no.	α [cm^{-1}]	n [-]	θ_s [-]	K_s [cm.hrs^{-1}]	S_s [cm^{-1}]	RMSE error (13) [cm]	
						$r_f = 0$	$r_f = 1$
1	2.447×10^{-4}	2.450	0.25	2.500×10^{-2}	4.190×10^{-3}	3.632×10^{-1}	
2	1.010×10^{-3}	2.651	0.271	1.092	2.879×10^{-2}	2.723×10^{1}	not computed
3	1.840×10^{-2}	2.098	0.353	1.092	1.845×10^{-4}	9.533×10^{-1}	
4	1.570×10^{-3}	1.968	0.720	2.070	1.053×10^{-5}	2.290×10^{-1}	
5	1.500×10^{-3}	1.586	0.720	1.093	7.641×10^{-5}	9.932	
6	2.775×10^{-3}	2.138	0.362	1.060	0	1.993×10^{-2}	1.363×10^{-2}
7	3.802×10^{-3}	1.279	0.594	1.165	0	9.694×10^{-3}	8.630×10^{-2}
8	2.550×10^{-3}	1.384	0.254	1.119	1.922×10^{-4}	1.030×10^{-2}	4.152×10^{-2}

treatment of the Richards equation, the numerical solver had exactly the same configuration as the one used for the reference solution.

Results of the synthetic problem are given in table 3. For these two different soil types involved the inverse modeling algorithm has found several local optima, and the low value of an objective function doesn't necessarily point to the correct solution. Thus the problem is multi-modal. Several distinct SHP parameter sets can lead to acceptable solutions. However, the most distinct SHP parameter is the saturated water content θ_s. It turns out that an expert knowledge is required here, to select an acceptable solution of this inverse problem.

4.2. Real-world problem

We found multiple optima for the real-world problem. The local extremes for the refinement level $r_f = 0$ are given in table 4, where the gray lines refer to local extremes with bad fitting properties (extremes 1-5), the local extremes 6-8 refer to inverse model solutions with good fitting properties. The results were visually inspected. An example of bad fitting dataset is depicted on figure 10 - left, and the example of the good fitting dataset is depicted on figure 10 - right. Solution for each dataset is given in Appendix. Complete settings specifications for each r_f level involved here are given in table 5.
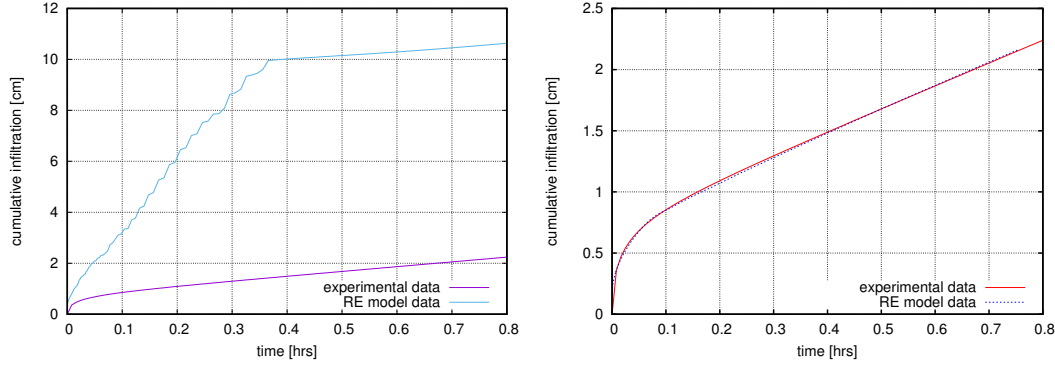
Figure 10: Left: Local extreme 2 – bad fitting properties, Right: Local extreme 5 – good fitting properties.

Table 5: Settings for different r_f levels. Computer architecture 32-core Intel(R) Xeon(R) CPU E5-2630, bogomips 4801.67, objective functions were evaluated in parallel.

r_f level	Picard criterion ε [cm]	number of nodes	number of elements	initial Δt [hrs]	CPU time for objective function computation [min]
0	$\leadsto +\infty$	2097	3861	10^{-6}	3
1	10^{-3}	4503	8488	10^{-7}	20
2	10^{-4}	9637	18588	10^{-8}	60

413   In the next step the refinement level was increased, new mesh was generated.

414   For the local extreme 6, the refined numerical treatment $r_f = 1$ didn't significantly update the positions of the

415 objective function (13) minima, see figure 11, and so this particular local extreme was confirmed after the first r_f

416 level update.

417   For the local extremes 7 and 8, the refined numerical treatment $r_f = 1$ significantly shifted with the objective

418 function (13), and new parameter search was enforced. The response plots of the objective function are depicted

419 in figures 12 and 13. The plots for the r_f=0 and r_f=1 with parametric set obtained at $r_f = 0$ level is depicted

420 with dashed lines. Following the methodology the new parameter search was conducted with Newton's method

421 with box-constraints (Byrd et al., 1995), where the initial parameter estimate was obtained from the solution at

422 previous r_f level given in table 4, and the parameters were searched within parametric subregions given in table 6.

423 The gradient algorithm converged fast and identified the updated solutions within less than 50 iterations. The new

424 updated solutions are in a close vicinity to the previous r_f level solutions. The response plots for the updated

425 refinement levels r_f=1,2 created with these updated solutions are depicted in figures 12 and 13 with continuous

426 lines.

427   For all evaluated extremes the response plots for r_f=1 and 2 have its minima nearby, and so it can be con-

428 cluded the extremes identified at r_f=1, were confirmed at refinement level $r_f = 2$. However, with the increasing

429 refinement level, the topology of the objective function becomes more complicated – non-smooth with more or

430 less significant oscillations. This effect becomes dominant on response plot depicted in figure 13 – top left. This

431 behavior originates from automatic time step selection, where the time step length is governed by both the trun-
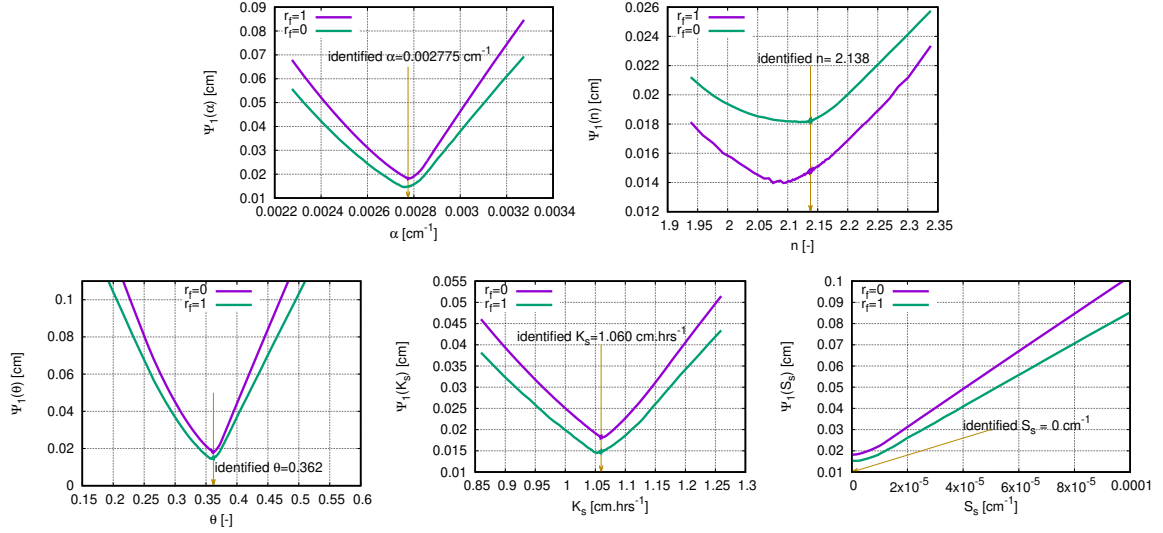
Figure 11: Response plots of the objective function (13) for the parameter α (top left), n (top right), θ (bottom left), K_s (bottom center), and S_s (bottom right) for extreme 6.

cation error and the nonlinear solver convergence rate. For low values of Picard criterion the solver becomes very sensitive on parameter updates. While changing the parametric values the solver requires slightly different temporal discretization, which in turn affects the objective function value. It turns out that for a refined nonlinear solver settings the straight forward application of a gradient solver could become troublesome. For the initial refinement level all response plots are smooth, and so the identified local extremes are free of these oscillatory attributes.

The final results of this parameter identification are summarized in table 7

Table 6: Ranges of SHP ($\mathbf{p}_{max}$ and $\mathbf{p}_{min}$) for identifying the SHP in the top-soil layer for refinement level $r_f = 1$.

extreme	θ_s [-]	α [cm^{-1}]	n [-]	K_s [cm.hrs^{-1}]	S_s [cm^{-1}]
7	0.445 - 0.742	2.852×10^{-3} - 4.753×10^{-3}	1.023 - 1.598	0.838 - 1.456	0.0 - 0.0
8	0.190 - 0.317	1.913×10^{-3} - 4.781×10^{-3}	1.038 - 1.730	0.839 - 1.398	1.440×10^{-4} - 2.400×10^{-4}

Table 7: The resulting SHP data sets.

no.	α [cm^{-1}]	n [-]	θ_s [-]	K_s [cm.hrs^{-1}]	S_s [cm^{-1}]	RMSE error (13) [cm]	
						$r_f = 1$	$r_f = 2$
6	2.775×10^{-3}	2.138	0.362	1.060	0	computed and confirmed at previous level	
7	3.800×10^{-3}	1.305	0.621	1.008	0	5.211×10^{-2}	1.217×10^{-2}
8	3.060×10^{-3}	1.364	0.243	1.067	1.920×10^{-4}	2.810×10^{-2}	3.066×10^{-2}

4.3. Limitations and realism of results

Local optima 7 resulted in the most realistic set for the podzolic top O+Ah soil layer, because of the most realistic value of θ_s, which is slightly higher than for the E horizon (table 1). Table 7 shows a wide range of θ_s
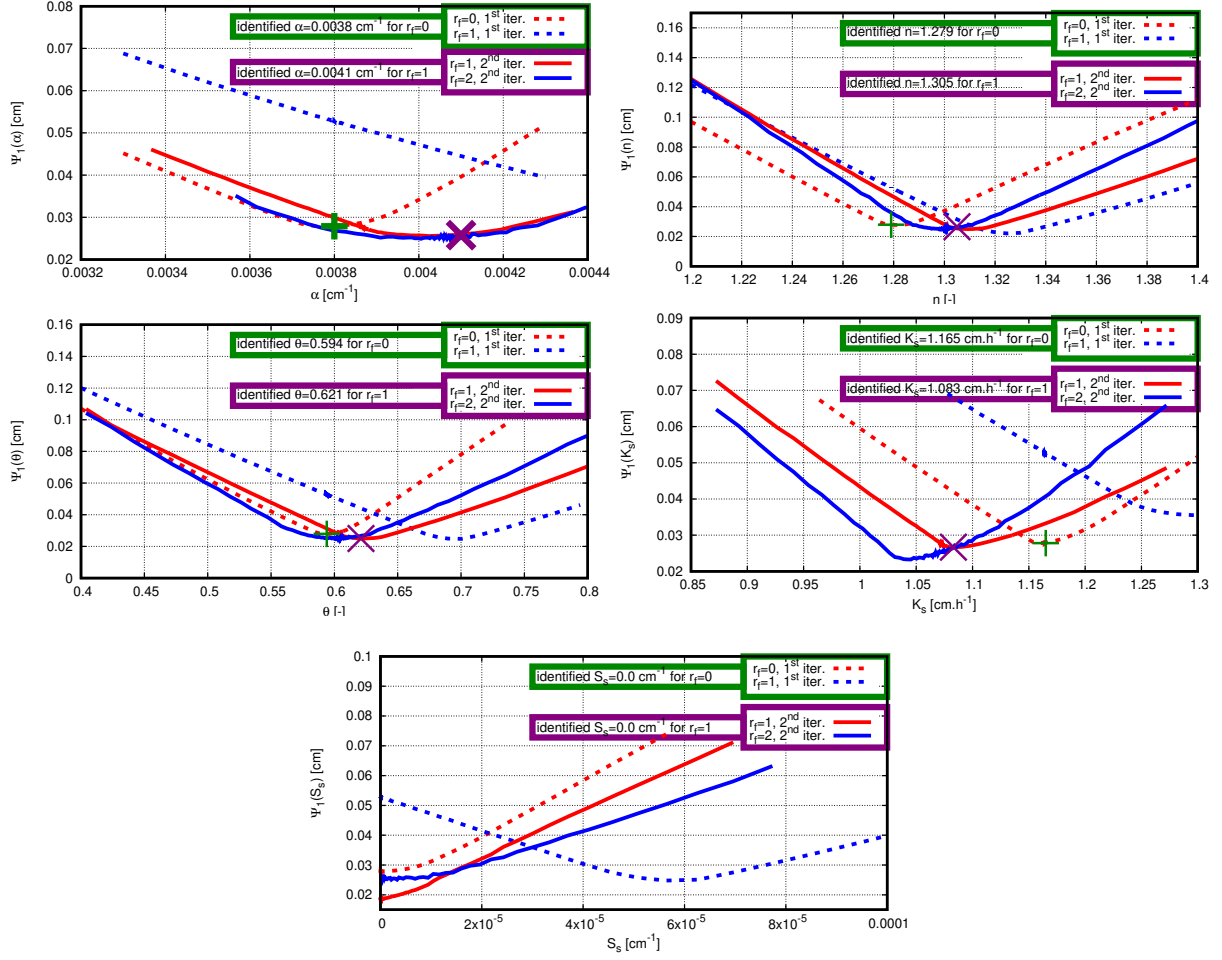
Figure 12: Response plots of the objective function (13) for the parameter *n* at extreme 7 (left) and S_s at extreme 8 (right)
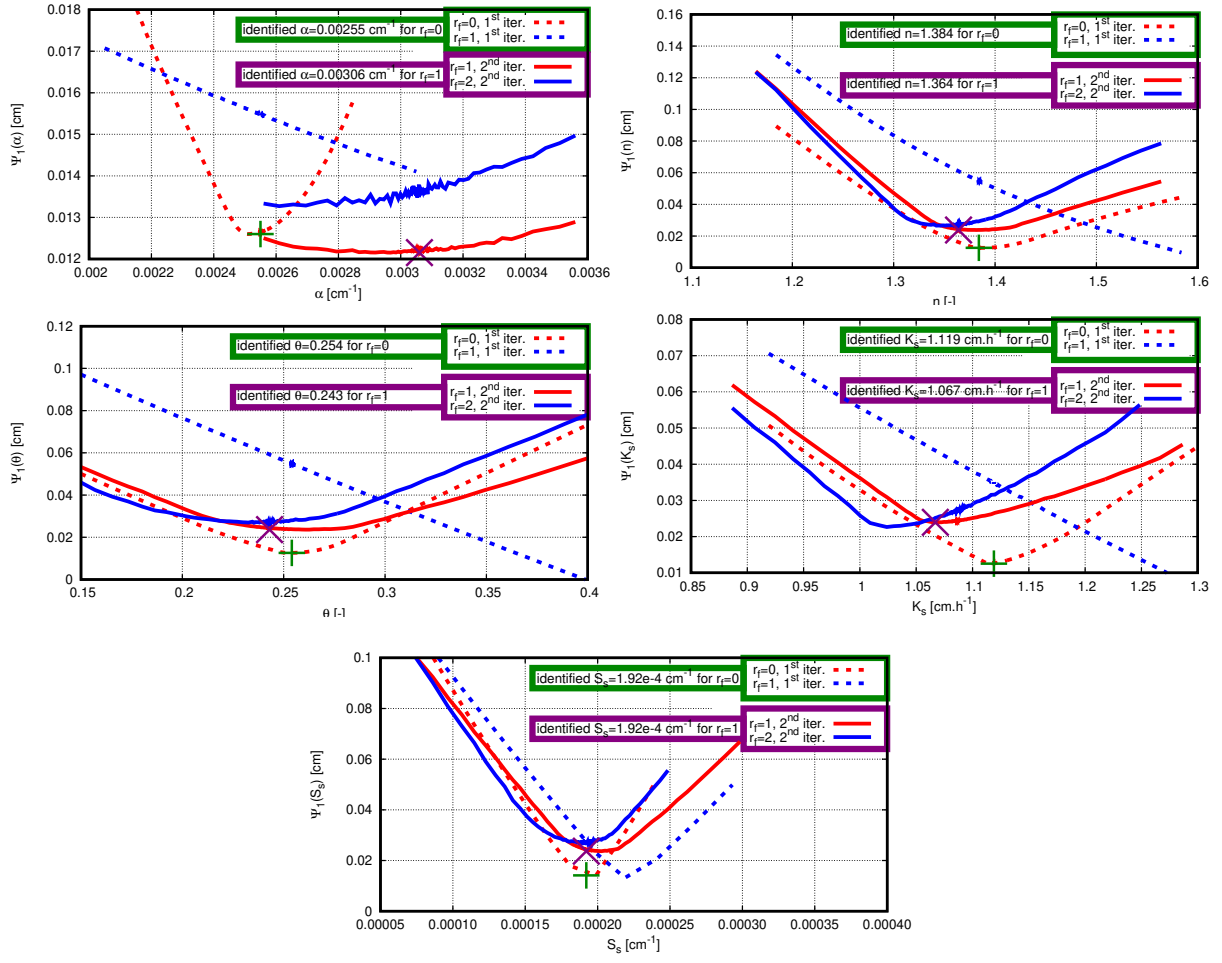
.

Figure 13: Response plots of the objective function (13) for the parameter n at extreme 7 (left) and S_s at extreme 8 (right)
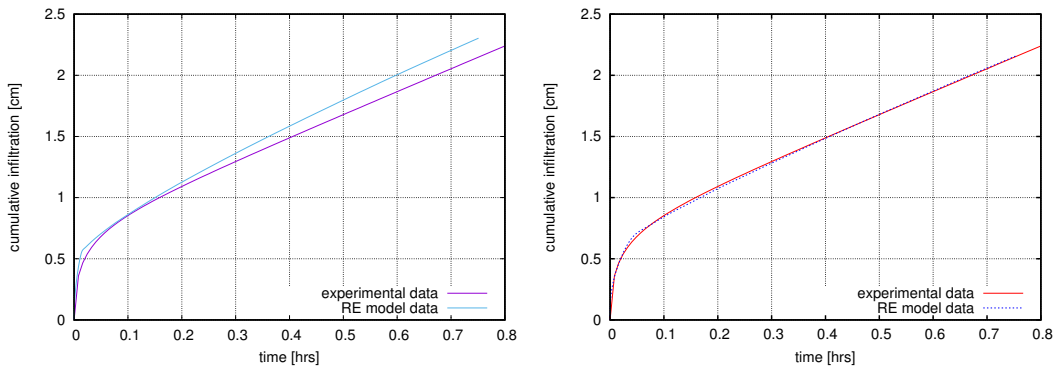
.

Figure 14: Left: Local extreme 7 infiltration curve for the original parameter set obtained at $r_f = 0$ and solved on model with discretization $r_f = 1$, right: solution for the updated parameter set in vicinity of the extreme 7.
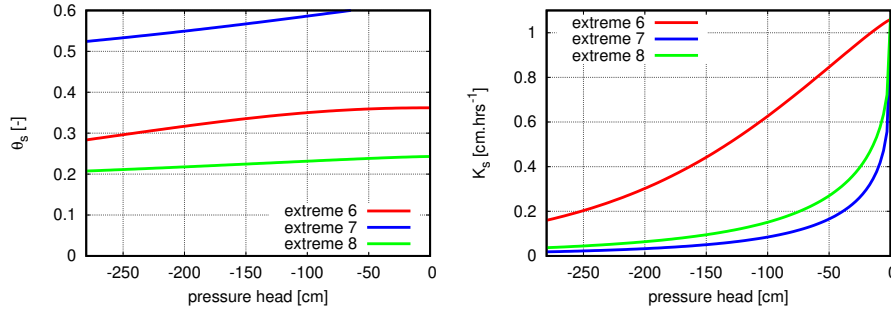
Figure 15: Left: Resulting retention curves obtained from the inverse model. Right:Resulting unsaturated hydraulic conductivity obtained from the inverse model.

values, which can have huge implications for the water storage of the soil. The saturated hydraulic conductivity K_s is similar across identified optima (table 7) and slightly lower than the lower horizon E (table 1). A physical explanation for the lower estimate can be that the O+Ah top layer can swell and air can be entrapped during infiltration and therefore, the volume of the effective pores can be decreased. This can be indicated by the lower values of θ_s. The identified K_s will be lower than the K_s fitted with the 1D Swartzendruber equation, because we are modeling 2D axisymmetric flow.

The identified values for α are also similar in range across the optima (table 7). α is related to the inverse of the air entry value, which in terms of suction is greater than the initial condition. Figure 15 shows that α barely impacts the shape of the retention curve in the modeled pressure head range, whereas θ_s and also n impact the retention curve significantly.

In the evaluation of the realism of the optimization we consider the treatment of the initial condition and the representativeness of the input curve as the greatest limitation. This however, does not delimit the applicability of the proposed calibration methodology.

5. Conclusions

We presented an automated calibration procedure that is able to identify optima from a relatively wide range of input parameters without convergence issues of the nonlinear operator. To solve the Richards equation we employed our open-source solver DRUtES (Kuraz et al., 2008). We also showed numerical considerations in the domain set-up of a challenging problem. We show that starting with the semi-explicit scheme can identify regions of interest. However, the identified SHP can change dramatically with an improved numerical set-up, so that several stages of refinement are required until SHP estimates can be confirmed. We also acknowledge that for this calibration to work, the optimization algorithm needs to be able to identify multiple optima.

We applied the methodology to synthetic and real transient SR infiltration data. Our synthetic infiltration problems show that identification of soils with unimodal grain size distribution can result in multiple distinct optima with good fitting properties. Although some optima show good fits, the parameters are not necessarily

physical/reasonable in the eyes of the expert. For both, the synthetic and real problems, expert knowledge on the saturated water content can aid the identification of the most reasonable optimum.

Improvements of the calibration methodology should include research on efficient numerical techniques to solve the Richards equation, such as the development of hp-adaptive approximations and adaptive domain decomposition methods.

References

R. Angulo-Jaramillo, J.-P. Vandervaere, S. Roulier, J.-L. Thony, J.-P. Gaudet, and M. Vauclin. Field measurement of soil surface hydraulic properties by disc and ring infiltrometers: A review and recent developments. *Soil Tillage Res.*, 55(1–2):1–29, 2000.

V. Bagarello, S. D. Prima, and M. Iovino. Estimating saturated soil hydraulic conductivity by the near steady-state phase of a beerkan infiltration test. *Geoderma*, 303(Supplement C):70 – 77, 2017.

J. Bear. *Hydraulics of groundwater*. McGraw-Hill series in water resources and environmental engineering. McGraw-Hill International Book Co., 1979.

A. Binley and K. Beven. Vadose zone flow model uncertainty as conditioned on geophysical data. *Ground Water*, 41(2):119–127, 2003.

D. Braess. *Finite elements: Theory, fast solvers, and applications in solid mechanics*. Cambridge University Press, 1997.

E. Buckingham. Studies on the movement of soil moisture. *USDA Bureau Soils – Bull.*, 38, 1907.

R. Byrd, P. Lu, J. Nocedal, and C. Zhu. A limited memory algorithm for bound constrained optimization. *SIAM J. on Sci. Comput.*, 16(5): 1190–1208, 1995.

M. A. Celia, E. T. Bouloutas, and R. L. Zarba. A general mass-conservative numerical solution for the unsaturated flow equation. *Water Resour. Res.*, 26(7):1483–1496, 1990.

Q. Cheng, X. Chen, X. Chen, Z. Zhang, and M. Ling. Water infiltration underneath single-ring permeameters and hydraulic conductivity determination. *J. Hydrol.*, 398(1–2):135–143, 2011.

I. Christie, D. F. Griffiths, A. R. Mitchell, and O. C. Zienkiewicz. Finite element methods for second order differential equations with significant first derivatives. *Int. J. for Numer. Methods Eng.*, 10(6):1389–1396, 1976.

N. Fodor, R. Sándor, T. Orfánus, L. Lichner, and K. Rajkai. Evaluation method dependency of measured saturated hydraulic conductivity. *Geoderma*, 165(1):60–68, 2011.

W. Gong, Q. Duan, J. Li, C. Wang, Z. di, A. ye, C. Miao, and Y. Dai. Multi-objective adaptive surrogate modeling-based optimization for parameter estimation of large, complex geophysical models. *Water Resour. Res.*, 52, 12 2015.

O. Hrstka and A. Kucerova. Improvements of real coded genetic algorithms based on differential operators preventing premature convergence. *Adv. Eng. Softw.*, 35(3):237 – 246, 2004.

S. I. Hwang and S. E. Powers. Estimating unique soil hydraulic parameters for sandy media from multi-step outflow experiments. *Adv. Water Resour.*, 26(4):445 – 456, 2003.

A. Ibrahimbegović, C. Knopf-Lenoir, A. Kucerova, and P. Villon. Optimal design and optimal control of structures undergoing finite rotations and elastic deformations. *Int. J. for Numer. Methods Eng.*, 61(14):2428–2460, 2004.

M. Inoue, J. Šimøunek, S. Shiozawa, and J. Hopmans. Simultaneous estimation of soil hydraulic and solute transport parameters from transient infiltration experiments. *Adv. Water Resour.*, 23(7):677 – 688, 2000.

L. Jačka, J. Pavlásek, M. Jindrová, P. Bašta, M. Černý, A. Balvín, and P. Pech. Steady infiltration rates estimated for a mountain forest catchment based on the distribution of plant species. *J. For. Sci.*, 58(12):536–544, 2012.

L. Jačka, J. Pavlásek, V. Kuráž, and P. Pech. A comparison of three measuring methods for estimating the saturated hydraulic conductivity in the shallow subsurface layer of mountain podzols. *Geoderma*, 219–220(0):82 – 88, 2014.

L. Jačka, J. Pavlásek, P. Pech, and V. Kuráž. Assessment of evaluation methods using infiltration data measured in heterogeneous mountain soils. *Geoderma*, 276:74 – 83, 2016.

M. T. Jensen. Helper-objectives: Using multi-objective evolutionary algorithms for single-objective optimisation. *J. Math. Model. Algorithms*, pages 323–347, 2004.

H. R. Kamali and S. Zand-Parsa. Optimization of a new inverse method for estimation of individual soil hydraulic parameters under field conditions. *Transactions of the ASABE*, 59(5):1257–1266, 2016.

P. Knobloch. On the choice of the supg parameter at outflow boundary layers. *Adv. Comput. Math.*, 31(4):369, Apr 2008.

J. D. Knowles, R. Watson, and D. W. Corne. Reducing local optima in single-objective problems by multi-objectivization. In *First International Conference on Evolutionary Multi-Criterion Optimization*, pages 269–283. Springer-Verlag. Lecture Notes in Computer Science No. 1993, 2001.

J. Kohne, B. Mohanty, and J. Simunek. Inverse dual-permeability modeling of preferential water flow in a soil column and implications for field-scale solute transport. *Vadose zone journal*, 5(1):59 – 76, 2006.

J. Kool, J. Parker, and M. Van Genuchten. Determining soil hydraulic properties from one-step outflow experiments by parameter estimation. i. theory and numerical studies. *Soil Sci. Soc. Am.*, 49:1348 – 1354, 1985.

M. Kowalsky, S. Finsterle, and Y. Rubin. Estimating flow parameter distributions using ground-penetrating radar and hydrological measurements during transient flow in the vadose zone. *Adv. Water Resour.*, 27(6):583–599, JUN 2004.

J. Kruis, K. Matouš, and Z. Dostál. Solving laminated plates by domain decomposition. *Adv. Eng. Softw.*, 33(7-10):445–452, 2002.

A. Kucerova. *Identification of nonlinear mechanical model parameters based on softcomputing methods*. PhD thesis, Ecole Normale Supérieure de Cachan, Laboratoire de Mécanique et Technologie, 2007.

M. Kuraz and P. Mayer. Algorithms for solving darcian flow in structured porous media. *Acta Polytecnica*, 53(4):347–358, 2013.

M. Kuraz, P. Mayer, M. Lepš, and D. Trpkošová. An adaptive time discretization of the classical and the dual porosity model of Richards' equation. *J. Comput. Appl. Math.*, 233:3167–3177, 2010. ISSN: 0377-0427.

M. Kuraz, P. Mayer, and J. R. Blöcher. DRUtES – an opensource library for solving coupled nonlinear convection-diffusion-reaction equations,, 2008. Development version 2018,
http://www.drutes.org .

M. Kuraz, P. Mayer, V. Havlicek, and P. Pech. Domain decomposition adaptivity for the richards equation model. *Comput.*, 95(1):501–519, 2013a.

M. Kuraz, P. Mayer, V. Havlicek, P. Pech, and J. Pavlasek. Dual permeability variably saturated flow and contaminant transport modeling of a nuclear waste repository with capillary barrier protection. *Appl. Math. Comput.*, 219(13):7127 – 7138, 2013b.

M. Kuraz, P. Mayer, and P. Pech. Solving the nonlinear richards equation model with adaptive domain decomposition. *J. Comput. Appl. Math.*, 270:2 – 11, 2014. Fourth International Conference on Finite Element Methods in Engineering and Sciences (FEMTEC 2013).

M. Kuraz, P. Mayer, and P. Pech. Solving the nonlinear and nonstationary richards equation with two-level adaptive domain decomposition

541   (dd-adaptivity). *Appl. Math. Comput.*, 267:207 – 222, 2015.

542   L. Lassabatère, R. Angulo-Jaramillo, J. M. Soria Ugalde, R. Cuenca, I. Braud, and R. Haverkamp. Beerkan estimation of soil transfer

543   parameters through infiltration experiments–best. *Soil Sci. Soc. Am. J.*, 70(7):521 – 532, 2006.

544   M. Leps. Parallel multi-objective identification of material parameters for concrete. In *Proceedings of the Ninth International Conference on*

545   *the Application of Artificial Intelligence to Civil, Structural and Environmental Engineering, Stirling: Civil-Comp Press Ltd*, 2007.

546   S. Mous. Identification of the movement of water in unsaturated soils: the problem of identifiability of the model. *J. Hydrol.*, 143(1):153 –

547   167, 1993. XVI General Assembly of the European Geophysical Society.

548   M. Nakhaei and V. Amiri. Estimating the unsaturated soil hydraulic properties from a redistribution experiment: Application to synthetic data.

549   *J. Porous Media*, 18(7):717–729, 2015.

550   C. Peña-Sancho, T. Ghezzehei, B. Latorre, C. González-Cebollada, and D. Moret-Fernández. Upward infiltration–evaporation method to

551   estimate soil hydraulic properties. *Hydrol. Sci. J.*, 62(10):1683–1693, 2017.

552   R Core Team. *R: A Language and Environment for Statistical Computing*. R Foundation for Statistical Computing, Vienna, Austria, 2017.

553   W. D. Reynolds. *Saturated hydraulic properties: Ring infiltrometer, in: Carter M.R., Gregorich, E.G. [Eds.], Soil Sampling and Methods of*

554   *Analysis, 2nd ed*. CRC Press Taylor & Francis, Boca Raton, USA, pp. 1043–1056, 2008a.

555   W. D. Reynolds. *Saturated hydraulic properties: Well permeameter, in: Carter M.R., Gregorich, E.G. [Eds.], Soil Sampling and Methods of*

556   *Analysis, 2nd ed*. CRC Press Taylor & Francis, Boca Raton, USA, pp. 1025–1042, 2008b.

557   L. A. Richards. Capillary conduction of liquids through porous mediums. *J. Appl. Phys.*, 1(5):318–333, 1931.

558   G. Roos, H., M. Stynes, and L. Tobiska. *Numerical Methods for Singularly Perturbed Differential Equations, Convection-Diffusion and Flow*

559   *Problems*. Springer-Verlag Berlin Heidelberg, 1996.

560   D. Rypl. Using the spherical harmonic analysis and the advancing front technique for the discretization of 3D aggregate particles. *Adv. Eng.*

561   *Softw.*, 41(1):38–45, 2010.

562   D. Rypl. *T3D Mesh Generator*. Department of Mechanics, CTU in Prague, Czech Republic, Prague, Czech Republic, 2004.

563   A. Saltelli, K. Chan, and E. Scott. *Sensitivity Analysis*. Wiley series in probabillity analysis. John Wiley & Sons, 2000.

564   D. Swartzendruber. A Quasi-Solution of Richards Equation for the Downward Infiltration of Water into Soil. *Water Resour. Res.*, 23(5):

565   809–817, MAY 1987.

566   M. T. van Genuchten, J. Simunek, F. J. Leiji, and M. Sejna. RETC, version 6.02 – code for quantifying the hydraulic functions of unsaturated

567   soils., 2009.

568   M. van Genuchten. Closed-form equation for predicting the hydraulic conductivity of unsaturated soils. *Soil Sci. Soc. Am. J.*, 44(5):892–898,

569   1980.

570   Z. Vitingerova. *Evolutionary Algorithms for Multi-Objective Parameter Estimation*. PhD thesis, CTU in Prague, Fac. of Civil Eng., 2010.

571   T. Weise, M. Zapf, R. Chiong, and A. J. Nebro. *Nature-Inspired Algorithms for Optimisation*, volume SCI 193, chapter Why Is Optimization

572   Difficult?, pages 1–50. Springer-Verlag Berlin Heidelberg, 2009.

573   X. Xu, C. Lewis, W. Liu, J. Albertson, and G. Kiely. Analysis of single-ring infiltrometer data for soil hydraulic properties estimation:

574   Comparison of best and wu methods. *Agric. Water Manag.*, 107(Supplement C):34 – 41, 2012.

575   A. Younes, T. Mara, M. Fahs, O. Grunberger, and P. Ackerer. Hydraulic and transport parameter assessment using column infiltration experi-

576   ments. *Hydrol. Earth Syst. Sci.*, 21(5):2263–2275, 2017.

577   Z.-Y. Zou, M. Young, Z. Li, and P. Wierenga. Estimation of depth averaged unsaturated soil hydraulic properties from infiltration experiments.

578   *J. Hydrol.*, 242(1–2):26 – 42, 2001.

Appendix A. Sensitivity analyses

The first procedure, which is typically required before proceeding the inverse modeling procedures, is the global sensitivity analyses on selected parameter ranges, see table 2. For simplicity the sensitivity analyses was conducted just for the first objective function (13). This strategy is in line with the statements given in the last paragraph of the section 2.4.1. In total 10.000 samples of the objective function (13) were evaluated, in order to obtain the Total Sobol Index for each parameter (Saltelli et al., 2000). The values of the Total Sobol Indices are given in table A.8. Since the evaluated Total Sobol Index for each parameter was nearly 0.9, our model exhibits an excellent sensitivity for all SHP parameters.

Table A.8: Total Sobol indices for the searched SHP parameters.

parameter	α	n	K_s	θ_s	S_s
Total Sobol Index	0.850	0.921	0.876	0.868	0.884

Appendix B. Solutions after the first identification run with $r_f = 0$ and $r_f = 1$.
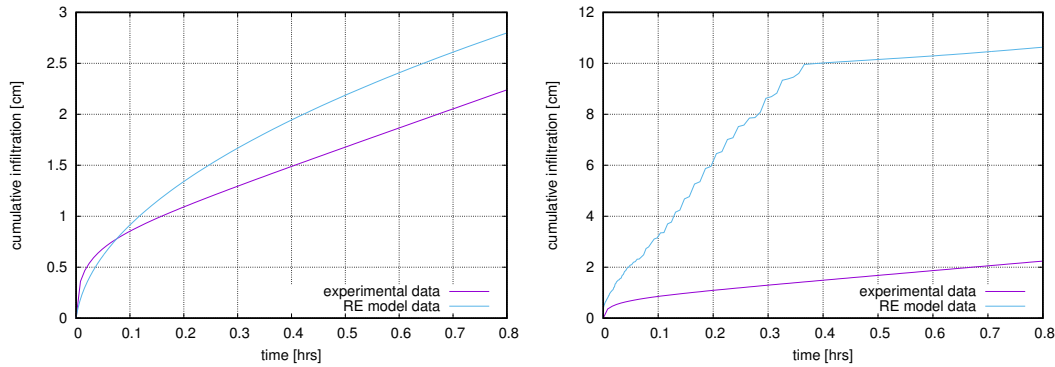

Figure B.16: Refinement level $r_f = 0$: Local extreme 1 , Right: Local extreme 2.

29

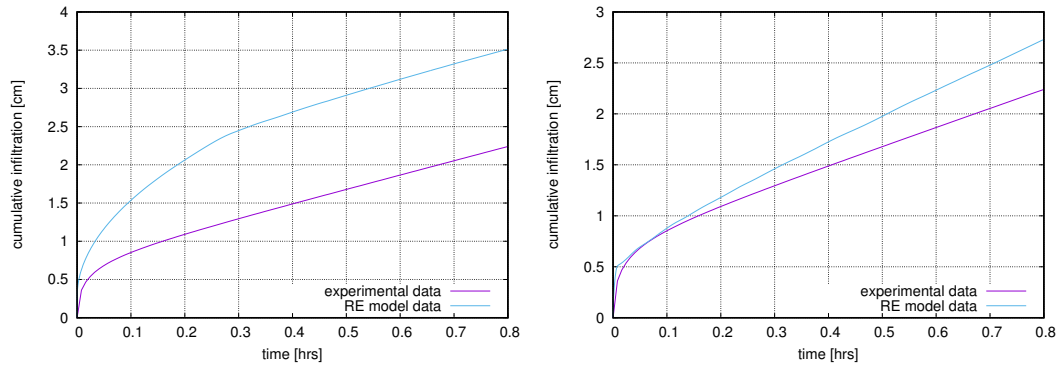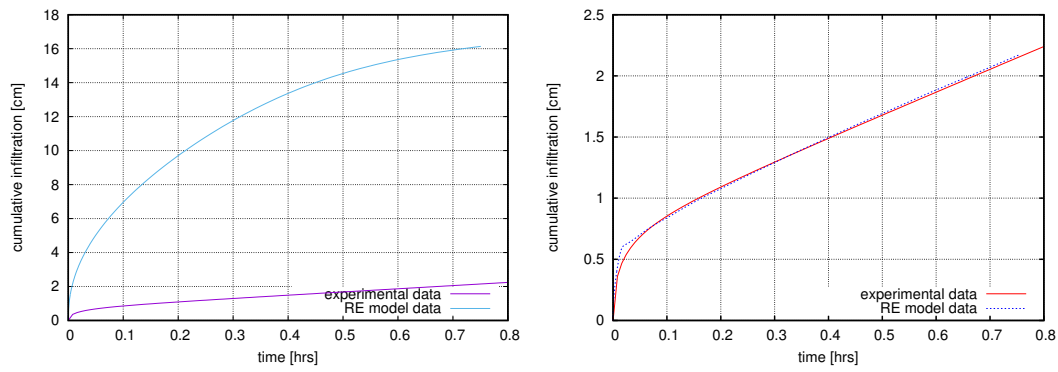Figure B.17: Refinement level $r_f = 0$: Local extreme 3 , Right: Local extreme 4.

Figure B.18: Refinement level $r_f = 0$: Local extreme 5 , Right: Local extreme 6.
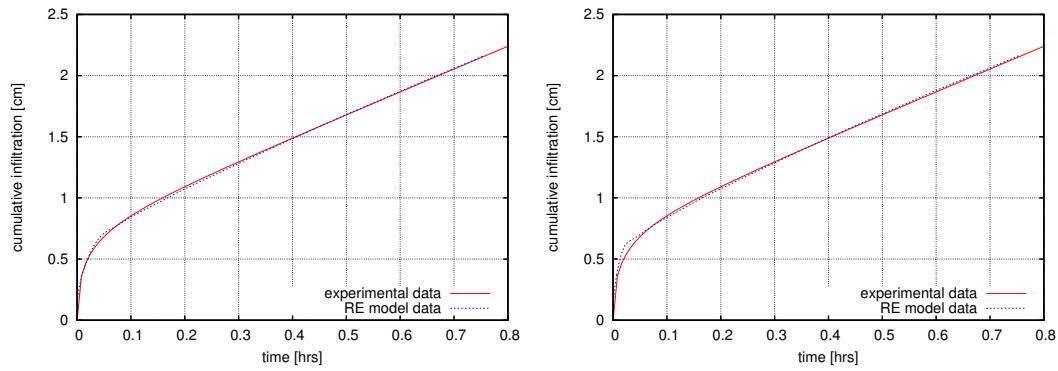

Figure B.19: Refinement level $r_f = 0$: Local extreme 7 , Right: Local extreme 8.